Research Article Vol. 14, No. 7 / 1 Jul 2023 / *Biomedical Optics Express* 3812

Biomedical Optics EXPRESS

Four-color fluorescence cross-correlation spectroscopy with one laser and one camera

SONALI A. GANDHI,[1] MATTHEW A. SANDERS,[2] JAMES G. GRANNEMAN,[2,3] AND CHRISTOPHER V. KELLY[1,3,*]

[1] *Department of Physics and Astronomy, Wayne State University, Detroit, MI 48201, USA*
[2] *Center for Molecular Medicine and Genetics, School of Medicine, Wayne State University, Detroit, MI 40201, USA*
[3] *Center for Integrative Metabolic and Endocrine Research, School of Medicine, Wayne State University, Detroit, MI 48201, USA*
[*] *cvkelly@wayne.edu*

Abstract: The diffusion and reorganization of phospholipids and membrane-associated proteins are fundamental for cellular function. Fluorescence cross-correlation spectroscopy (FCCS) measures diffusion and molecular interactions at nanomolar concentration in biological systems. We have developed an economical method to simultaneously monitor diffusion and complexation with the use of super-continuum laser and spectral deconvolution from a single detector. Customizable excitation wavelengths were chosen from the wide-band source and spectral fitting of the emitted light revealed the interactions for up to four chromatically overlapping fluorophores simultaneously. This method was applied to perform four-color FCCS that we demonstrated with polystyrene nanoparticles, lipid vesicles, and membrane-bound molecules. Up to four individually customizable excitation channels were selected from the broad-spectrum fiber laser to excite the diffusers within a diffraction-limited spot. The fluorescence emission passed through a cleanup filter and a dispersive prism prior to being collected by a sCMOS or EMCCD camera with up to 1.8 kHz frame rates. The emission intensity versus time of each fluorophore was extracted through a linear least-square fitting of each camera frame and temporally correlated via custom software. Auto- and cross-correlation functions enabled the measurement of the diffusion rates and binding partners. We have measured the induced aggregation of nanobeads and lipid vesicles in solution upon increasing the buffer salinity. Because of the adaptability of investigating four fluorophores simultaneously with a cost-effective method, this technique will have wide application for examining macromolecular complex formation in model and living systems.

© 2023 Optica Publishing Group under the terms of the Optica Open Access Publishing Agreement

1. Introduction

Fluorescence correlation spectroscopy (FCS) and fluorescence cross-correlation spectroscopy (FCCS) are powerful techniques to reveal the diffusion behavior of molecules at nanomolar concentration in model and biological systems [1–7]. FCS and FCCS provide single-molecule sensitivity to reveal the average diffusive characteristics through a confocal detection volume [8–10]. As fluorescently labelled molecules diffuse through a detection volume, the fluctuating fluorescent signals are obtained and correlated [11,12]. The fluorescence emission intensity versus time varies depending on the number and brightness of the fluorophores as they enter and leave the observation volume [13–16]. FCS reveals biophysical parameters of a single-color channel, including the molecular diffusion coefficients and concentrations by analyzing the autocorrelation dwell time (τ_D) and amplitude (G_0). The comparison of multiple color channels occurs with fluorescence cross-correlation spectroscopy (FCCS) [17] during which the molecular interactions and co-diffusion are measured [2,11]. If distinctly labelled particles are bound

#486937 https://doi.org/10.1364/BOE.486937
Journal © 2023 Received 2 Feb 2023; revised 14 Apr 2023; accepted 18 Apr 2023; published 29 Jun 2023

together as they diffuse through the observation spot, then their fluorescence intensities have simultaneous fluctuations and their cross-correlation amplitude is large [18].

FCS and FCCS typically examine fluorescence emission with an acquisition rate of ≤10 kHz and <10 μW of excitation light focused to a diffraction-limited observation spot. The fluorophores are excited and emit thousands of times as they diffuse through the observation volume. For this purpose, a sensitive detector and well-chosen fluorophores with complementary excitation and emission spectrums are prerequisites. Fluorophores with high absorption cross-sections, high quantum efficiencies, and resistance to photobleaching are desired to obtain 10-1000 collected photons during their microsecond transit through the detection volume [3].

To observe molecular binding with FCS the bound and unbound states must typically have diffusion coefficients that vary by >2x, which is rare upon ligand binding or dimerization [19,20]. FCCS overcomes this limitation by detecting free diffusors and aggregates through multi-color correlations [21,22]. For FCCS, binding molecules are labelled with chromatically distinct fluorophores and the cross-correlation of the corresponding detection channels reveals their co-diffusion [21,23,24]. Generally, the emission of all diffusers is obtained simultaneously with the same experimental conditions [2].

Traditional, FCCS is limited to the observation of various fluorophores that are well chromatically separated to minimize the fluorescence emission bleed-through detected in the wrong channel [25,26]. Typically, the color channels are chromatically separated through dichroic mirrors and channel-specific emission filters prior to each channel's detection in a dedicated avalanche photodiode or photomultiplier tube. Bleed-through between the color channels often yields a non-zero cross-correlation for independently diffusing fluorophores and difficulty in observing molecular binding events. Crosstalk between color channels is especially problematic when fluorescent proteins are used, and each fluorophore's emission spectrum is wide.

To overcome this complicating spectral cross-talk, the pulsed interleaved excitation (PIE) FCCS method has been developed where excitation and detection of each fluorophores occurs at unique time points [17,27]. In addition to separating the emission spectrally as in standard multicolor FCCS, temporal separation via picosecond pulsed excitation single photon emission counting provides greater fluorophore resolution [28]. However, this technique often requires numerous fluorophore-specific detectors and pinhole alignments for each emission channel. Prism and diffraction grating-based FCCS simplify the detection path of the FCCS experiment by spectrally separating the emission light [2,23,29]. EMCCDs provide single-fluorophore detection, but typically the background noise of EMCCDs prohibits single-photon detection [2]. Four-color FCCS has been previously implemented with photomultiplier tube arrays [24,26], but we are not aware of prior uses of EMCCDs for four-color FCCS.

This manuscript reports on a new FCCS method that can resolve up to four spectrally overlapping fluorophores to study their mobility and clustered interactions with a single excitation source and a single detector. This method simultaneously measures the intensity versus time of four fluorophores to be analyzed as four autocorrelations, six two-color cross-correlations, and up-to five higher-order cross-correlations. The advantage of multicolored FCCS is that it enables measurement of molecular density and diffusion rates for four populations. In addition, the emission from four channels is also useful to calculate cross-correlation between the pairs to determine binding. This novel method uses a single super-continuum laser as an excitation source that provides multiple excitation wavelengths dependent on the choice of excitation filters. A single confocal aperture and dispersive prism play vital roles by reducing out-of-focus fluorescence emission to enhanced SNR and chromatically spread emission on single sensor that obviate the need of multiple detectors, respectively. The article provides details on the experimental setup and demonstrates its capability to resolve four fluorescent polystyrene nanobeads and three fluorescently labelled lipid vesicles in solution. FCCS revealed that the nanobeads and the lipid vesicles initially diffused independently with negligible cross-correlations. Upon increasing the buffer ionic strength or the addition of bovine serum albumin (BSA), the nanobeads and the lipid vesicles aggregated into multi-colored diffusers with significant cross-correlations. Further, single-molecule detection has been verified by revealing the independent diffusion of membrane-bound fluorescent proteins and fluorescently labeled phospholipids. Future adaptations of this method will provide resolution and interactions of the intricate binding and unbinding events of membrane-bound proteins.

2. Materials and methods

2.1. Sample preparation

Typically, single-color fluorescent nanobeads were mixed together and diluted with milli-Q water (>18 MΩ cm). The most frequently used nanobeads include 100-nm diameter blue beads with an excitation wavelength (λ_{ex}) of 450 nm (Fluoro-Max; Fisher Scientific); 100-nm diameter yellow bead with $\lambda_{ex} = 515$ nm (FluoSpheres; Life Technologies); 100-nm diameter red bead with $\lambda_{ex} = 561$ nm (Fluoro-Max; Fisher Scientific); or 40-nm diameter dark red bead with $\lambda_{ex} = 635$ nm (FluoSpheres, Life Technologies). The mixture of nanoparticles was placed on a glass bottom dish (MatTek) after the dish was rinsed with ethanol and dried in a nitrogen stream.

Large unilamellar vesicles (LUVs) were composed of non-fluorescent phospholipids and fluorescent phospholipids. The primary, non-fluorescent component of the LUVs was 1,2-dioleoyl-sn-glycero-3-phosphocholine (DOPC; Avanti Polar Lipids). LUVs included one of three trace fluorescent lipids: 1-palmitoyl-2-(dipyrrometheneboron difluoride) undecanoyl-sn-glycero-3-phosphocholine (TF-PC, Avanti Polar Lipids); 1,2-dipalmitoyl-sn-glycero-phosphoethanolamine Texas Red (DPPE-TR, Life Technologies); 1,2-dioleoyl-sn-glycero-3-phosphocholine-N-Cyanine 5 (DOPC-Cy5, Avanti Polar Lipids). DOPC (99.98 mol%) and TF-PC, DPPE-TR, or DOPC-Cy5 (0.02 mol%) in chloroform were mixed in glass vial. Lipids were dried under a nitrogen stream and kept in vacuum for >30 min. The lipid film was hydrated to 1 mg/mL with milli-Q water (<18 mΩ cm). The solution was vortexed and extruded eleven times through membrane filter with a 100 nm pore size within an extruder (LiposoFast, Avestin). The procedure was repeated to yield independent stock solutions for each color LUVs before they were mixed in single vial to examine their independent or correlated diffusion.

For CTxB diffusion, supported lipid bilayers (SLBs) were prepared by bursting giant unilamellar vesicles (GUVs) upon a glass coverslip. GUVs of 1-palmitoyl-2-oleoyl-sn-glycero-3-phosphocholine (POPC; Avanti Polar Lipids) and 0.3 mol % GM1 Ganglioside (Avanti Polar Lipids) were prepared by electro-formation, as described previously [30–33]. Exposing the GUVs on plasma-cleaned coverslips resulted in their bursting and created continuous bilayer. CTxB was labeled with AlexaFluor 647 or AlexaFluor 488 before purchase (Thermo Fisher Scientific). CTxB was added to the SLB for a final concentration of 0.25 mg/mL above the SLB to saturate all available GM1. After 0.5 min of incubation, the unbound CTxB was rinsed away.

The phospholipid monolayers of the artificial lipid droplets (aLDs) were formed from multilamellar vesicles (MLVs) composed of non-fluorescent DOPC and 0.05 mol% fluorescent DOPC-Cy5. The phospholipids were mixed in chloroform, dried under a nitrogen stream, kept under vacuum for >30 min. The dried phospholipid film was hydrated to a concentration of 0.1 mg/mL Intracellular Buffer (IB) and lightly vortexed to obtain MLVs. IB consists of 10 mM HEPES, 140 mM KCl, 6 mM NaCl, 1 mM $MgCl_2$, and 2 mM EGTA within milli-Q water. The MLVs were mixed with glyceryl trioleate (TO; Millipore Sigma) at a mass ratio of 1000:1 TO:PL and bath sonicated for 30 min (Ultrasonic Cleaner 96043-936; VWR Symphony) to form aLDs. aLDs were mixed with 20-µm diameter nonfluorescent polystyrene beads (Millipore Sigma) and purified proteins, as needed, prior to being sandwiched between a glass slide and a coverslip (Fisher Scientific), which were previously cleaned and passivated. Details for the protein purification are given in the Supplemental Material. In this system, the nonfluorescent beads acted as spacers to prevent the coverslip and the glass slide from getting too close together and smashing the aLDs. The glass slides and coverslips were rinsed with ethanol, dried under nitrogen stream, and passivated with casein. Passivation included exposing the slides and coverslips to 20 mg/mL of casein in milliQ water for >20 min prior to rinsing with milli-Q water [34]. 7 µL of the aLD, bead, and protein mixture was sandwiched between a glass slide and coverslip as the final stage in sample preparation. The buoyant aLDs floated at the top of the sandwich, which was the glass slide while the coverslip was closer to the inverted microscope objective. The bottom of the aLDs, the "south pole," was the focus for the FCCS observation point such that neither the illumination nor emission light had to refract through the aLD on its path to or from the objective.

2.2. *Optical setup*

The four-color FCCS was performed with a customized inverted microscope (IX71, Olympus) on a vibration isolated optical table. Excitation was provided by a super-continuum fiber laser (SC-Pro, YSL photonics) that produced broad spectrum pulsed laser with wavelengths ranging from 400 nm to 2400 nm. For safety, the long-wavelength component (>650 nm) was separated by a dichroic mirror and blocked within a light-tight box to reduce the total laser power present during the free-space customization of the fluorescence excitation paths. The optical colors were separated by dichroic mirrors, chromatically filtered (BrightLine FF02-435/40, FF01-513/13, FF01-561/14, and FF01-630/38, Semrock), expanded, attenuated, and recombined. Each excitation color had <10 µW average power. The combined excitation channels were reflected by a three-band dichromic mirror (ZT442/514/561rpc, Chroma) and directed into a 40x, 1.30 NA microscope objective (UIS2 BFP1, Olympus) to a focused point in the sample. The emission from the diffraction-limited illumination point was collected by the same objective, passed through the three-band dichroic mirror, transmitted through the emission filter (ZET442/514/561 m, Chroma), and focused by the microscope tube lens through a 40-µm diameter confocal pinhole (P40D, ThorLabs). The emission was transmitted through a relay lens (Optomask, Andor) that was customized with the insertion of a chromatically separating prism (PS812-A, ThorLabs). The emission was collected on the center pixels of either an EMCCD camera (iXon Ultra 897, Andor) or sCMOS camera (Zyla, Andor) with the emission chromatically spread on the camera sensor (Fig. 1). This setup provided a 16 nm color difference per pixel for the EMCCD and 6.6 nm color difference per pixel for the sCMOS. We achieved improved signal-to-noise by applying 2 × 2 binning and data points corresponding to 13.2 nm chromatic differences for the sCMOS images without causing significantly worse spectral fitting. Alternatively, a linear array of photomultiplier tubes or single-photon counting modules could have been used with potentially superior performance and cost effectiveness for new builds. We chose to use the camera sensors because they were readily available in our lab, as we expect they are in other labs as well. Both the confocal pinhole and the camera were placed on 3D translation stages (PT3, Thorlabs) to allow for precise alignment. This setup has integrated computer control of the connected with camera and real-time correlations with custom Python routines (LabVIEW, National Instruments).

The excitation beams required precise alignment and determination of the size of illumination volume. We used the control sample of a fluorescent supported lipid bilayer (SLB) illuminated by each focused excitation beam to ensure consistent illumination alignment. SLBs provided a uniform fluorophore distribution such that the fluorescence image without a pinhole showed the shape of the illumination. The image of the excitation light on the SLB was fitted to a 2D Gaussian function to determine the width of laser spot (w_0) (Fig. S1). To confirm the 3D confocal volume, the diffusion of 100-nm diameter fluorescent polystyrene particles was compared to expected results, as detailed within the Supplemental Material. The diffusion coefficient (D) was calculated theoretically, $D = k_B T/(3\pi\eta d)$, and measured experimentally, $D = {w_0}^2/(4\tau_D)$, which incorporates Boltzmann's constant (k_B), temperature (T), solvent viscosity (η), particle diameter (d), and

Biomedical Optics EXPRESS

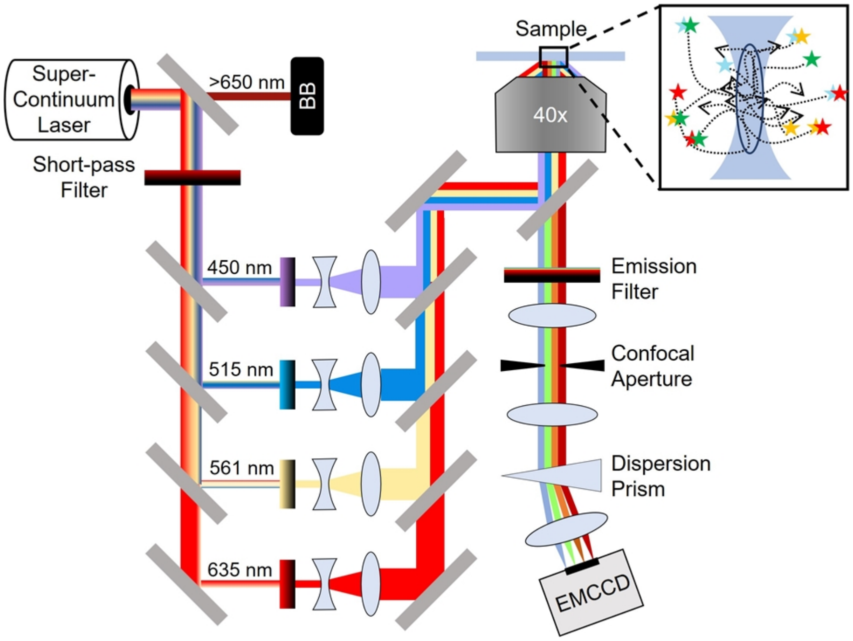

Fig. 1. The FCCS set up included a super-continuum laser that was separated into four narrow-spectrum excitation channels that travelled through clean-up filters, neutral density filters, and beam-expanding telescopes prior to being recombined. The combined excitation colors were passed through the microscope objective to illuminate a diffraction-limited volume within the sample. The fluorescence emission was collected by the objective, passed through an emission filter and a pinhole before being focused on the camera sensor. (Inset) Four fluorescently labelled species diffusing independently or as an aggregate through the confocal detection volume yield independent or correlated emission intensities.

dwell time (τ_D). The theoretical and experimental values of D for 100-nm diameter polystyrene microspheres in water were consistent, $D = 4.39$ μm^2/s and 4.45 ± 0.06 μm^2/s, respectively [35].

Samples were exposed to <10 μW total excitation power with $\lambda_{ex} = 450$, 515, and 561 nm. The optical setup also provides a 635 nm excitation, but the fluorophores with >680 nm emission used in these experiments were sufficiently excited by the shorter wavelength excitation such that the 635 nm excitation was not used here. All camera parameters were set to maximize their frame rate. The choice of exposure time was a balance of fast acquisition and signal-to-noise to yield the best fitting of the correlation functions. For the EMCCD, we used the frame transfer mode, cropped sensor mode, and the maximum 17 MHz pixel readout rate. For single fluorophore diffusers, each frame was acquired with a 0.3-ms exposure at a 1,785 Hz frame rate on the EMCCD. The EMCCD could have provided up to 3,678 Hz frame acquisition rate if a 0.2-ms exposure would have provided sufficient signal. Each frame required an acquisition time during which the emission was not collected. Typically, 53,550 frames were acquired per 30-sec acquisitions for the 496×4 pixel ROI with the EMCCD for FCCS. For the sCMOS, we used the rolling shutter, a 540 MHz pixel readout rate, and a 5-ms exposure time. These parameters yielded a 196 Hz frame rate and 5,876 frames per 30-sec acquisition for a 20×4 pixel ROI. The sCMOS could have provided a 26,041 Hz frame acquisition rate if a 1 μs exposure time would have been sufficient. Longer exposure times were necessary for the sCMOS versus the EMCCD to obtain sufficient signal-to-noise considering the greater read noise of the sCMOS compared to the EMCCD. These frame rates were sufficient to measure the diffusion of membrane-bound molecules or >40 nm diameter diffusers in solution for which diffusion rates are typically <10 μm^2/s. However, the frame rates were not sufficient to measure small molecule diffusion in aqueous suspension for which diffusion rates are typically >100 μm^2/s.

Both cameras were set to their low operating temperature, which was -80 °C for the EMCCD with recirculating liquid cooler and -10 °C for the sCMOS. Both cameras demonstrated heating during these fast acquisitions that warranted consideration to ensure the cooling mechanisms and the sensor were within tolerance. The recirculating water cooler was essential for the EMCCD running at its maximum rate with the EM gain set to 150.

2.3. Extraction of I versus T

Each image was averaged over the dimension perpendicular to the chromatic separation to isolate the emission spectrum from all fluorophores at a moment in time. This spectrum versus time was analyzed to extract the relative changes to each fluorophore's concentration within the observation spot versus time. Extraction of each fluorophore's concentration required determining the expected emission spectrum from each fluorophore and fitting each acquired spectrum to a linear combination of the spectra from the present fluorophores. The linear fitting of the detected spectrum to the sum of expected emission spectrum to each fluorophore has been done previously [2,36], but we incorporated two rounds of computational correction for unavoidable sub-pixel misalignment in our day-to-day optical setup. This approach provides distinct detection of each fluorophore despite their highly overlapping spectra with a combination of non-linear spectrum fitting, non-linear fitting of optical alignment imperfections, and a linear deconvolution of the collected spectrum into a linear combination of the single-fluorophore spectra.

The fluorescence emission spectrum for each fluorophore was collected from control samples that each contained one fluorophore while excited by all excitation colors (Fig. 2(A)-(D), S2A-C). To account for day-to-day sub-pixel misalignment, the single-fluorophore spectra were each fit to the sum of three Gaussians to provide a continuum model of each fluorophore's emission after the three-band dichroic mirror and emission filter (Figs. 2(F), S2E),

$$Em_{fit}(\lambda,\ \lambda_0) = \sum_{i=1}^{3} A_i e^{\frac{-(\lambda-\lambda_0-\lambda_i)^2}{2\,\sigma_i^2}}. \tag{1}$$

This fitting function was chosen because it provided a smooth, analytical fit to the collected points of the single-fluorophore emission spectra with fewer fitting parameters than other candidate fit functions; there was not a physical meaning for this three-Gaussian fit. Equation (1) provided a continuous function that represented the spectrum of each fluorophore used. The nine fit parameters of amplitude (A_i), center (λ_i), and width (σ_i) were identified for each fluorophore and unchanged during later fits. The fitting parameter λ_0 was shared by all three Gaussians and allowed for the emission spectra for each fluorophore to be effectively shifted on the sensor to account for day-to-day sub-pixel variations in optical alignment. Another control sample was created with well-resolved intensities of M different fluorophores simultaneously to determine the relative shift of the calibration files with a separate λ_0 for each fluorophore (λ_0^{Fluor}) (Figs. 2(E), (F), S2D, (E)) according to

$$S_{fit}(\lambda) = \sum_{Fluor=1}^{M} I_{Fluor} Em_{fit}^{Fluor}(\lambda,\ \lambda_0^{Fluor}) + I_{dark}. \tag{2}$$

When fitting the sum of each fluorophore's Em_{fit} (Em_{fit}^{Fluor}) to this multi-colored control sample the relative shift (λ_0^{Fluor}) and the amplitude (I_{Fluor}) of each Em_{fit}^{Fluor} were identified. Later fits kept λ_0^{Fluor} fixed because λ_0^{Fluor} represents the inherent relative emission spectrum of each fluorophore. The dark counts on the detector, which were approximately 2% of the signal, were subtracted during fitting by the incorporation of a constant (I_{dark}).

The system required sample-specific sub-pixel alignment. A shift of the emission spectra was determined for each sample while keeping the relative shift for each fluorophore constant. For

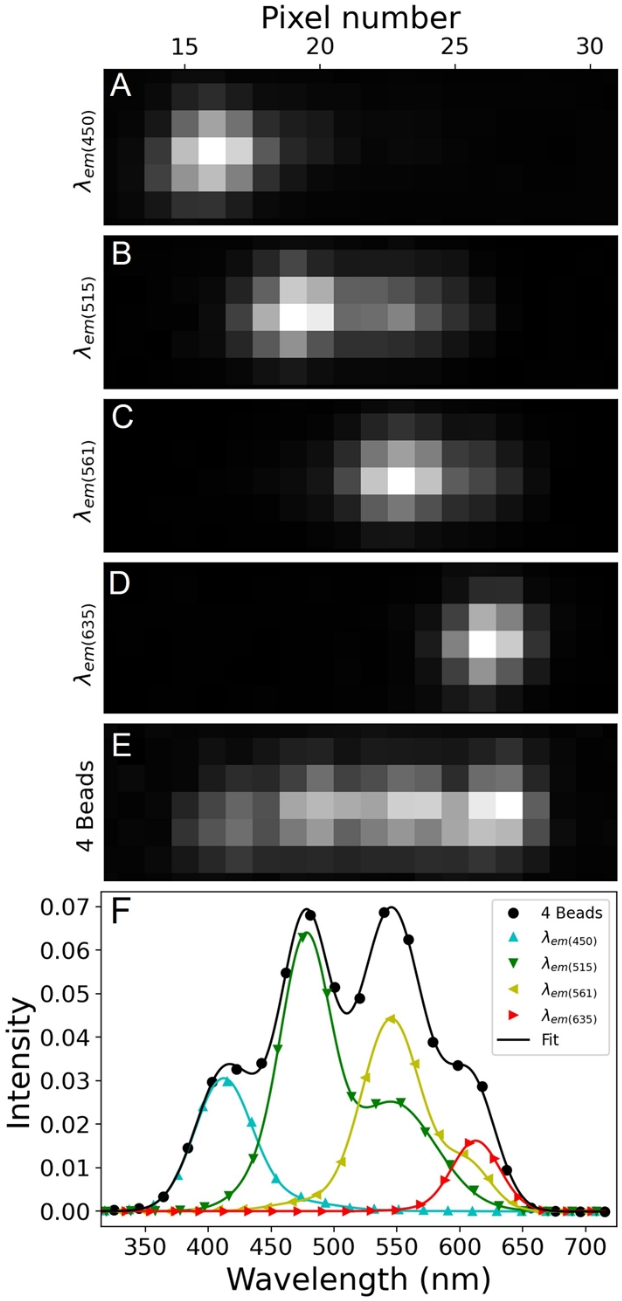

Fig. 2. Chromatic separation of emission spectrum on the camera sensor. Spectrally overlapping emission of fluorescent nanobeads was dispersed via prism was collected on the camera. (A-D) Single nanobeads of excitation wavelengths 450, 515, 561 and 635 nm, respectively, were spectrally separated and collected on the cropped ROI. For this demonstration, the ROI was 18×6 pixels. Each column of pixels on the camera is associated with an emission wavelength. (E) Samples with all four nanobeads show the distinct, but highly overlapping emission spectra. (F) Control samples with only one color of bead present were used to identify the emission spectrum of each bead type (*colored symbols and fits*). With four nanobeads simultaneously present, the spectrum was fit to reveal the emission intensity of each bead type for each camera frame (*black symbols and fit*).

each sample, the time-averaged sample spectrum was fit with a single shared shift for all Em_{fit}^{Fluor} corresponding to the sample-specific chromatic shift on the camera sensor during acquisition according to

$$S_{fit2}(\lambda) = \sum\nolimits_{Fluor=1}^{M} I_{Fluor} Em_{fit}^{Fluor}(\lambda,\ \lambda_0^{\mathrm{Fluor}} + \lambda_0^{Sample}) + I_{dark}. \tag{3}$$

The analysis did not benefit from including a time-varying fit shift of the emission spectra for each camera frame, which would have accounted for alignment shifts during the 30-sec acquisition if present. The sample-specific sub-pixel calibration shifts reduced the unexpected positive and negative cross-correlation amplitudes. Through the above, multi-step method, many variables are set precisely to well-resolved spectra such that the potentially noisy experimental spectra from a single camera frame with highly discrepant fluorophore concentrations could be fit with minimal fitting unknowns; only the intensity of each fluorophore unknown and fit to each camera frame in the experimental data.

With the shifted continuous fluorophore emission spectra identified, the expected intensity from each fluorophore on each camera pixel was determined and linear least squared fitting was performed to each camera frame to provide the intensity of each fluorophore at each moment in time. Linear least squared fitting provides 100x improved computational efficiency and indistinguishable auto- and cross-correlation results from a nonlinear least square fitting of the continuous sum of Em_{fit}^{Fluor} to the experimental spectra.

2.4. Data analysis

The autocorrelation (G^{Auto}) of each intensity versus time signal revealed the diffusive behavior via the correlated intensity versus lag time (τ) of a single species according to

$$G^{Auto}(\tau) = \frac{\langle \delta I(t)\ \delta I(t+\tau)\rangle}{\langle I(t)^2\rangle}, \tag{4}$$

where $I(t)$ represents the time average intensity. In FCCS, two emission intensities versus time are analyzed via cross-correlation (G^{Cross}) according to

$$G^{Cross}(\tau) = \frac{\langle \delta I_1(t)\ \delta I_2(t+\tau)\rangle}{\langle I_1(t)\rangle\ \langle I_2(t)\rangle}, \tag{5}$$

The auto and cross-correlation were fit to the expected correlation decay of homogeneous 2D or 3D Brownian diffusion (Eq. (6) or (7)) to extract the correlation amplitude (G_0) and τ_D [37] according to

$$G_{Fit\ 2D}\ (\tau) = 1 + \frac{G_0}{1 + \frac{\tau}{\tau_D}}\ , \tag{6}$$

$$G_{Fit\ 3D}\ (\tau) = 1 + \frac{G_0}{1 + \frac{\tau}{\tau_D}\ \sqrt{1 + \left(\frac{r_0}{z_0}\right)^2 \frac{\tau}{\tau_D}}}\ , \tag{7}$$

Equation (7) incorporates the radial (r_0) and axial (z_0) distances over which the intensity decay by 1/e^2, the immersion oil index of refraction ($n = 1.518$) and the numeric aperture of the objective (NA = 1.30), as further described in the Supplemental Material [38]. The acquired intensity versus time traces were checked for photobleaching and significant stage drift before fitting to Eqs. (6) or (7).

G_0 for autocorrelations (G_0^{Auto}) reports the number of diffusers in the detection volume ($N \propto 1/G_0$) with a strong dependence on the background incorporated into the signal. Interpretation of the magnitudes of cross-correlations (G_0^{Cross}) was performed by calculating the fraction of correlated (F_c), according to

$$F_c = \frac{2\ G_0^{Cross}}{G_0^{Auto1} + G_0^{Auto2}} \tag{8}$$

3. Results

3.1. *Comparison of sCMOS vs EMCCD cameras*

The read noise of sCMOS is low compared to EMCCD, but the dark counts were lower, and the quantum efficiency was greater for the EMCCD. Both the sCMOS and EMCCD cameras worked well to detect the transit of bright diffusers that had multiple fluorescent molecules each (*i.e.*, the nanobeads and the LUVs). However, the EMCCDs provided superior signal-to-noise for the single-fluorophore diffusers (*i.e.*, the single proteins or lipids). Both cameras enabled sufficient hardware and software for this method, but with our need for a system that is suited for many sample types and the challenges of switching between cameras, we chose to primarily use the EMCCD.

3.2. *Induced aggregation of nanobeads*

The diffusion and aggregation of the fluorescent nanobeads or LUVs were measured in aqueous suspensions. Four distinct types of polystyrene nanobeads were measured with peak excitation wavelengths of 450, 515, 561, or 635 nm (B_{450}, B_{515}, B_{561}, or B_{635}). Three different types of LUVs were labeled with TopFluor-PC (TF), DPPE-Texas Red (TR), or DOPE-Cy5 (CY5) with peak excitation wavelengths of 515, 561, or 647 nm (L_{515}, L_{561}, or L_{647}). Nanobeads or LUVs were mixed, and their fluorescence emission intensities were collected for 30 sec at >1.7 kHz. Intensities versus time for each channel showed many small and uncorrelated events that reflect independent diffusion of each species (Figs. 3(A), S3A). The average of 27 sequential measurements of autocorrelations for four channels were calculated and fit to yield τ_D for each bead type (Fig. 4(B)), which were in accordance with the expected values for the varying size beads (Table 1). In ultrapure water, the cross-correlations between the nanobeads were negligibly small or negative (Figs. 3(C), 4(C)).

Table 1. Comparison of beads' diffusion, diameter, and aggregate fraction.

Bead type	Quoted diameter (nm)	D_{Theory} (µm²/sec)	D_{Exp} (µm²/sec)		Estimated diameter (nm)		Aggregate fraction (%)
			Water	PBS	Water	PBS	PBS
B_{450}	100	4.39	4.45 ± 0.06	0.71 ± 0.05	98.7 ± 1.2	618.7 ± 40	99.9
B_{515}	100	4.39	2.86 ± 0.03	0.92 ± 0.07	153.9 ± 1.4	477.5 ± 30	99.7
B_{561}	100	4.39	3.44 ± 0.02	0.80 ± 0.06	127.7 ± 0.6	547.7 ± 40	94.4
B_{635}	40	10.98	7.09 ± 0.06	1.00 ± 0.06	61.9 ± 0.5	439.3 ± 20	97.5

Upon increasing the salinity of the solution by the addition of PBS, the nanobeads randomly bound together as the salts encouraged aggregation. The four intensities versus time showed many correlated peaks confirming the formation of large, multicolored nanobead clusters (Fig. 3(d)). Upon aggregation, the autocorrelations showed longer decay times as the diffusion slowed (Figs. 3(E), 4(b)). This is best demonstrated by comparing normalized autocorrelations with water or PBS; increasing salinity caused the beads to clump and diffuse slower (Fig. 4(a)). Additionally, the cross-correlations displayed significantly increased G_0^{Cross} and F_C as the binding increased. (Figure 3(f), 4(c)).

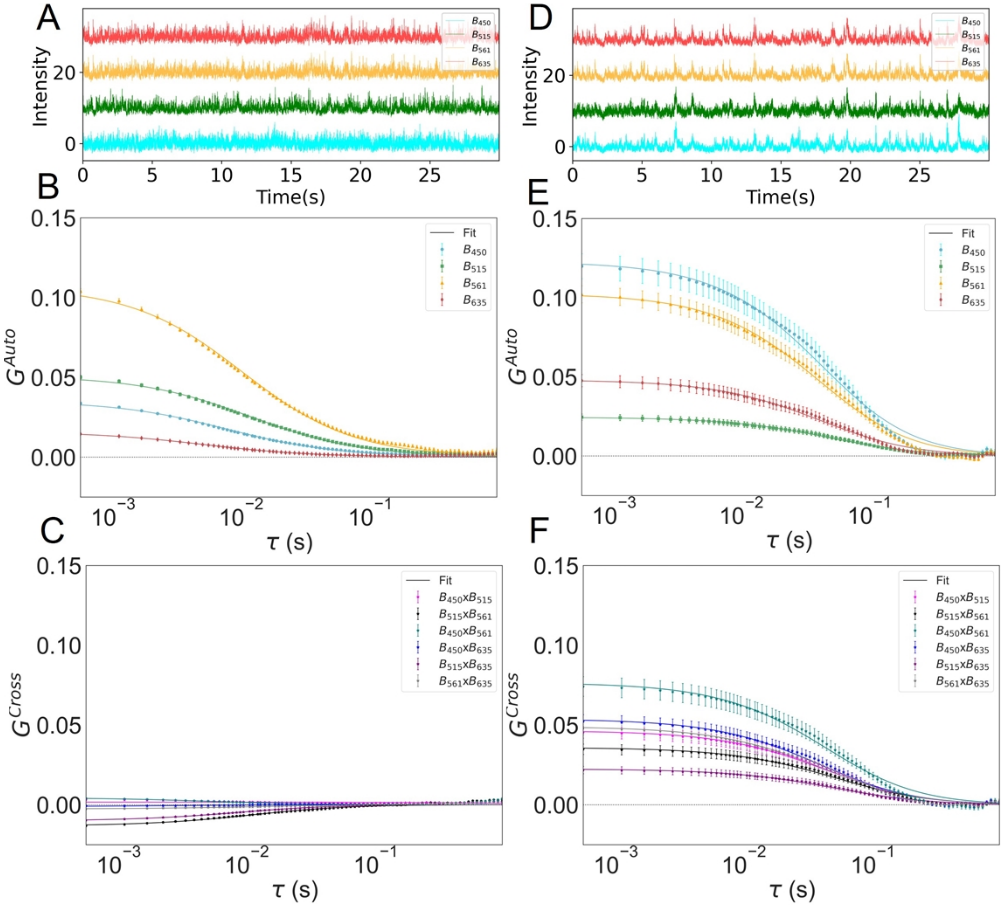

Fig. 3. FCCS on four spectrally overlapping nanobeads. (A) Fluctuations in intensity versus time for four nanobeads (B450, B515, B561, B635) show many small uncorrelated peaks that indicate the nanobeads are diffusing independently. The results were analyzed with (B) auto and (C) cross-correlations. (B) The autocorrelations were well resolved and (C) the cross-correlations were small or negative. The addition of PBS induced aggregation of nanobeads. (D) The intensity versus time for the four-color channels showed many events with correlated peaks because the nanobeads formed clusters and were diffusing together. PBS yielded both the (E) auto- and (F) cross-correlations increased to display increased amplitudes and dwell times. (B, C, E, F) Symbols and error bars represent the mean and standard error of the mean for >20 sequential measurements while the lines represent the fits from Eq. (7).

3.3. Nanobeads aggregate composition

The composition of the aggregates was examined by recognizing that the autocorrelations with PBS included information about both monomeric and aggregated diffusers within a sample. The autocorrelations in water provide the diffusion dynamics of only the monomers. The cross-correlations in PBS provide the diffusion dynamics of only the aggregates. The autocorrelations in PBS include the dynamics of both the monomers and the aggregates as a reflection of the polydispersity of the sample. Accordingly, we fit the autocorrelation in PBS to be a linear sum of the autocorrelation in water and the cross-correlation in PBS such that the relative amplitudes of the components reflected the fraction of the diffusers that were monomers vs aggregates,

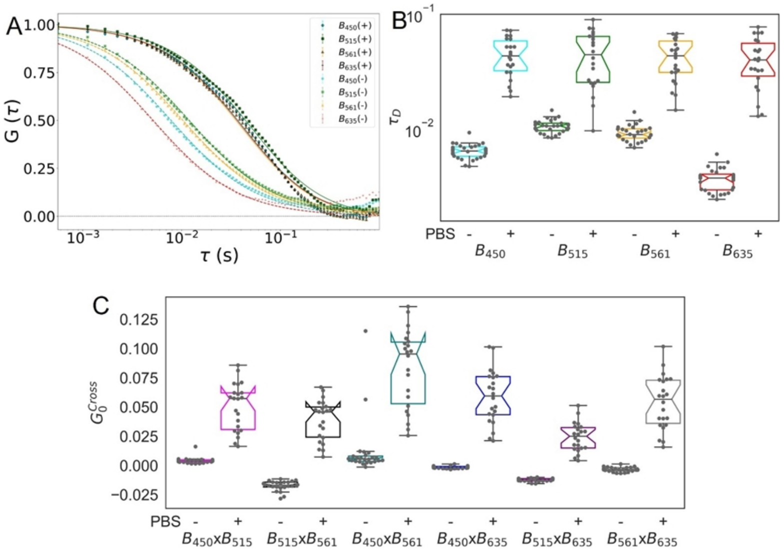

Fig. 4. (A) The normalized autocorrelations in water and PBS for the four nanobeads simultaneously observed. A minus sign (-) indicates the absence of PBS and the plus sign (+) indicates the presence of PBS. (B) The autocorrelations displayed slower diffusion upon the addition of PBS and (C) the cross-correlations displayed larger amplitudes upon the addition of PBS, which demonstrates that multi-colored aggregates had been formed.

according to

$$G_{PBS}^{Auto} \approx G_{Poly} = \frac{G_0^{Mono}}{1 + \frac{\tau}{\tau_D^{Auto,\ Water}} \sqrt{1 + \left(\frac{r_0}{z_0}\right)^2 \frac{\tau}{\tau_D^{Auto,Water}}}} + \frac{G_0^{Agg}}{1 + \frac{\tau}{\tau_D^{Cross,PBS}} \sqrt{1 + \left(\frac{r_0}{z_0}\right)^2 \frac{\tau}{\tau_D^{Cross,PBS}}}} - 1. \quad (9)$$

This approach assumes that the aggregates and the monomers each have distinct dwell times, which is supported by the high-quality fitting of the correlations, but a heterogeneous population of aggregate likely exists. The resulting G_0^{Mono} and G_0^{Agg} were used to calculate the fraction aggregated according to

$$f_{Agg} = G_0^{Agg} / (G_0^{Mono} + G_0^{Agg}) \quad (10)$$

and listed within Table 1. We observed all four nanobeads displayed f_{Agg} above 94%, with B_{450} having f_{Agg} equal to 99.9%. Analysis of the bead monomer and aggregate diffusion coefficients, the aggregate diameters were estimated to be 520 ± 90 nm, which was 6x larger than that of the monomeric beads. This indicates that over 200 nanobeads joined into a single aggregate (Table 1). Similarly, we observed all three LUVs displayed f_{Agg} above 77% (Table S2). The Stokes-Einstein relationship was used to connect the diffuser diameter to diffusion coefficient while assuming a solution viscosity of 1 cP and temperature of 20 °C.

3.4. *Induced aggregation of lipid vesicles*

Three-color FCCS was also performed on LUVs that incorporated three highly overlapping fluorescent lipids, as described above. The fitting of continuous functions to the individual fluorophore's spectra, shifting the fits to accommodate optical misalignments, and the linear least squared fitting processes described above effectively separated the combined spectra for extraction of each fluorophore's intensity vs time (Fig. S2). Our observations were like the nanobeads in that the LUVs were diffusing independently in water (Fig. S3A, B). With the

LUVs, aggregation was induced by the addition of BSA at 30 g/L to the buffer (Fig. S3C, D), and heteroaggregation was detected through the strong cross-correlations.

3.5. Membrane-bound protein diffusion on lipid bilayers

To evaluate the sensitivity of our system to single, membrane-bound molecules, we examined membrane-bound fluorescent proteins of cholera toxins (CTxB). CTxB are soluble proteins that bind to the glycolipid GM1 incorporated into phospholipid membranes. The CTxB that was labeled with the synthetic, bright AlexaFluor (AF) dyes were successfully perform with either the sCMOS or EMCCD camera. An SLB sample with both CTxB-AF488 and CTxB-AF647 bound displayed independent diffusion of the two populations of CTxB and no cross-correlation (Fig. 5(a, b)).

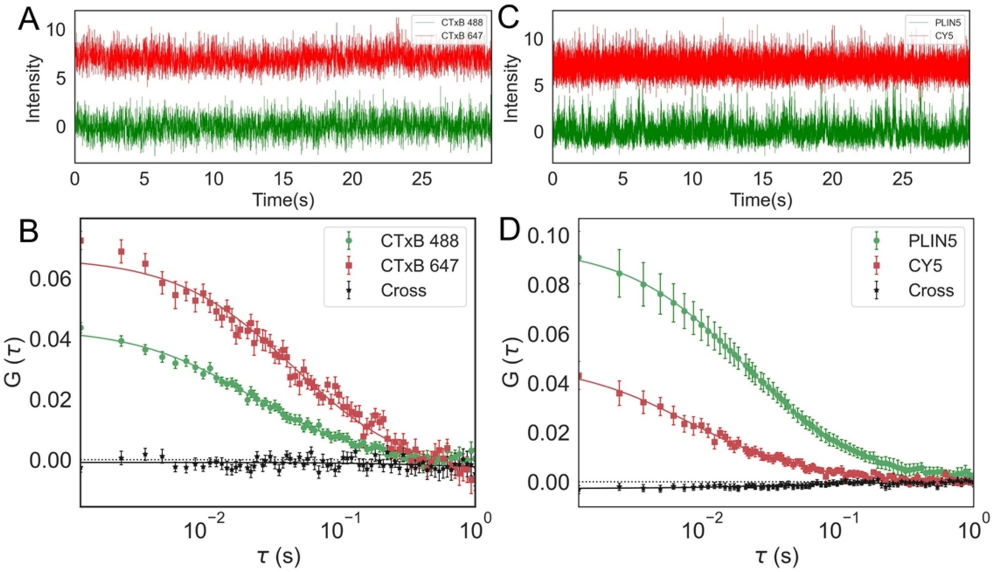

Fig. 5. Protein-protein and protein-lipid diffusion on phospholipid bilayer and monolayer were detected by our FCCS system. (A) The intensity versus time curves of two proteins CTxB-AF488 and CTxB-AF647 were analyzed to yield (B) two autocorrelations and cross-correlation of these bilayer-bound proteins. No apparent association between the two distinct populations of CTxB was observed. (C) The intensity versus time PLIN5-YFP and DOPE-CY5 were analyzed to yield (D) two autocorrelations and a cross-correlation of the monolayer-associated molecules. PLIN5-YFP and DOPE-Cy5 diffused independently on surface of lipid monolayer. Symbols and error bars represent the mean and standard error of the mean for >25 sequential measurements while the lines represent the fits from Eq. (6).

3.6. Independent protein and phospholipid diffusion on lipid monolayer

To evaluate the capability of our system to measure the diffusion on the phospholipid monolayer surface of an aLD, we examined the diffusion of a fluorescent phospholipid (DOPE-Cy5) and a purified lipid droplet scaffolding protein labeled with a yellow fluorescent protein (PLIN5-YFP). FCCS was performed on the “south pole” of the aLDs and revealed no cross-correlation between DOPE-Cy5 and PLIN5-YFP. The autocorrelations demonstrated that DOPC-Cy5 was diffusing 2x faster than PLIN5-YFP, and the cross-correlations were negligible (Fig. 5(c, d)).

4. Discussion

With only one laser source and one detector, this custom FCCS method reveals four distinct color channels as part of a novel experimental and computational routine. No cross-correlations were observed for independent diffusers despite highly overlapping spectra. FCCS data are important for providing information on the mobility, concentration, and diffusion dynamics through the analysis of autocorrelations. Amplitudes of autocorrelations are inversely proportional to number of diffusers in observation volume. Also, τ_D can be quantified in each of auto- and cross-correlations that gives residence time of diffusers in the detection volume. In addition, the multicolored clusters can be evaluated by analyzing cross-correlation amplitudes.

All the nanobeads were moving independently to each other in ultrapure water; cross-correlations did not give positive amplitudes. Small and negative cross-correlation magnitudes between the beads in ultrapure water were analyzed for potential excluded volume effects, spectral bleed through, physical bead sizes, and surface chemistry of the beads. An excluded volume effect may have contributed to the negative cross-correlations (*i.e.*, $G_0^{Cross}<0$). The presence of one 100-nm diameter bead within the 300-nm wide observation volume likely reduced the probability of other beads in the observation volume simultaneously, thus the negative correlation between beads [2,39]. However, comparing beads of differing diameter did not show a clear correlation between bead sizes and G_0^{Cross}, thus no evidence was found for the excluded volume effect contributing to our negative cross-correlations. (Fig. 6).

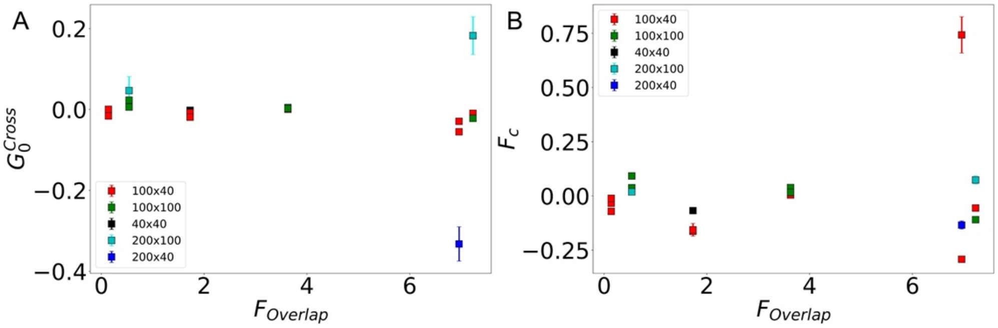

Fig. 6. Fractional overlapping of the wavelengths versus bead parameters. (A) $F_{Overlap}$ versus G_0^{Cross} for combination of bead sizes (B) Fraction correlated (F_C) for varying bead sizes plotted against $F_{Overlap}$.

The induction of nanobead aggregation with addition of PBS shows increase in G_0 in all six pairs of cross-correlations (Fig. 4(C)). The larger amplitude means fewer independent diffusers, consistent with the individual diffusers clumping together to form multicolored clusters. G_0 for autocorrelations also increased, except for B_{515} (Fig. S4). Upon aggregation, τ_D increased 1.8 ± 0.7 ms, with B_{635} having maximum 3.00 ± 0.03 ms increase compared to ultrapure water τ_D for same beads (Fig. 4(B)).

To examine the contribution of spectral overlap to the observed cross-correlation, we computed fractional spectral overlap ($F_{Overlap}$) between each pair of beads according to

$$F_{Overlap}^{i,j} = \int_0^\infty Em_i * Em_j \, d\lambda. \tag{11}$$

Em_i is the normalized emission spectrum for bead i. $F_{Overlap}$ ranged from 0.14% to 7.23% while G_0^{Cross} was between -0.35 to 0.18. There was no correlation between $F_{Overlap}$ and G_0^{Cross} for any of the nanobeads (Fig. 6(A)). As expected far wavelengths had less spectral overlapping than the closer ones, but they had no greater G_0^{Cross} or F_C for bead of varying physical sizes (Fig. 6(B)). Further the anti-cross-correlation which might be the cause of bleed through between the channels, but we do observe the negative cross-correlation for channels $B_{450}xB_{635}$ which is 450 nm and 635 nm emission channels that has negligible ($F_{Overlap} = 0.14\%$) bleed through between them. So, Bleed through cannot lead to anti-cross-correlation.

Moreover, to access surface chemistry of the beads, the beads' surfaces were coated either with uncharged polystyrene or were negatively charged carboxylate coated (Table S1). None of the combinations of bead surface chemistries showed any significant trends for . We found no trends for the observed negative cross-correlation with dependences on the bead color, spectral overlap, size, or surface chemistry.

To investigate the possibility for data analysis artifacts being the source of anti-cross-correlation, we developed diverse computational routines to ensure a robust and accurate extraction of each fluorophore's intensity versus time. For example, we ensured that fluctuations in the laser intensity did not influence our results by calculating the autocorrelation of the laser intensity when the attenuated laser was directly detected on our camera. The autocorrelation of the laser showed no significant correlations at any of the lag times accessible by our camera. Similarly, we examined the auto- and cross-correlations of the background intensity (I_{dark}) when I_{dark} was determined in each camera frame. A disadvantage of using cameras for FCCS detection is the large background intensity inherent to the system. However, no auto- or cross-correlations were observed with I_{dark} and any of the fluorophore intensities. Relatedly, no differences in the fluorophore data were observed when I_{dark} was fit to a constant over the full 30-sec acquisition versus being allowed to vary and independently fit to each camera frame. We performed the control analysis of trying to extract intensities versus time for fluorophores that were not present in our sample. By including excess calibration functions to our intensity extraction, the other intensities versus time were unaffected. Finally, we tested if the simultaneous fitting of all intensities versus time provided different results than fitting the fluorophore intensities sequentially. In brief, it was essential that we fit all fluorophore intensities simultaneously to accurately correct for chromatic bleed through. Without simultaneous fitting, false positive cross-correlations were observed.

The four intensities present for four beads allowed us to examine if all beads contributed similarly to the aggregation. Three and four intensities were correlated to acquire two and three lag times between them, respectively (Eqs. S1, S2). The 2D plot of cross-correlation matrix showed τ_1 and τ_2 are independent and perpendicular to each other for nanobeads in PBS (Fig. S5) [40]. Three nanobeads were chosen at a time for this analysis to assess association and dissociation between macromolecules of interest and assess if the interaction of any two bead types were key to the larger, multi-color aggregation. We did not observe the key large multicolored aggregation between the nanobeads or in LUVs (Fig. S6) via double or triple cross-correlation analysis, but this quantification routine can be useful for the future experiments that needs to examine multi-color protein aggregation and complex assembly.

In sum, our FCCS has diverse applications on a variety of samples including live cells, lipid monolayers, and lipid bilayers. Like all free-space FCCS setups, this system includes the potential for misalignment of the lasers, the pinhole, camera, and drift in focus, all of which can lead to noisy autocorrelations and false-negative cross-correlations. But which can be tackled by following strict experimental and statistical routines for system alignment. We have demonstrated the ability of this method to independently detect up to four spectrally overlapping fluorophores without false-positive cross-correlations. Our camera-based system is sensitive enough to detect single-fluorophores, but the relatively slow camera frame rate compared to conventional FCS detectors limits the detection of small molecules in solution with $D > 20\ \mu m^2/s$.

5. Conclusions

In this study, we developed a multi-color FCCS system that demonstrated interaction and diffusion dynamics of four spectrally overlapping fluorescent probes. Our economical FCCS uses multiple laser channels in the excitation path that were created from single supercontinuum laser

(400-700 nm) and a dispersive prism that gave the emission spectra of multiple chromatically overlapping fluorophores on to a single detector. Camera-based FCCS allows increases the accessibility of FCCS by no longer requiring unique, expensive detectors for each color channel while simultaneously overcoming the false-positive cross-correlation due to spectral bleed through. Measurements of diffusion time and fluorophore density were successfully performed on polystyrene fluorescent nanobeads. Also, on the same nanobeads system FCCS enabled us to observe induced aggregation and clustered interaction caused due to addition of PBS. Measurement of diffusion coefficient clearly showed long decay time and slower diffusion in presence of PBS due to formation of multicolored aggregates. Due to the adaptiveness of detecting four molecules simultaneously, our FCCS is conventional to use with fluorescent proteins and lipids in biological model and live systems. Moreover, the ability to calculate full triple cross-correlation decay, the size of the three-color species can be possible to determine via FCCS. The advantage of the system will be investigation of diffusion simultaneously with same experimental conditions on multiple fluorophores that will also save multiple sample preparation and experiment time. Future experiments will include up to four lipolysis associated proteins and phospholipids, that will be examined on the surface of monolayers. This approach will be used to investigate triple cross-correlation decay and can identify complex assembly and disassembly kinetics.

Funding. Directorate for Mathematical and Physical Sciences (DMR1652316); National Institute of Diabetes and Digestive and Kidney Diseases (R01DK076629); the Richard Barber Interdisciplinary Research Program.

Acknowledgements. We thank Susheel Pangeni, Abir Kabbani, Xinxin Woodward and Nasser Junedi for valuable discussions.

Disclosures. The authors declare no conflicts of interest.

Data Availability. Data underlying the results presented in this paper are not publicly available at this time but may be obtained from the authors upon reasonable request.

Supplemental document. See Supplement 1 for supporting content.

References

1. F. Schneider, P. Hernandez-Varas, B. C. Lagerholm, D. Shrestha, E. Sezgin, M. J. Roberti, G. Ossato, F. Hecht, C. Eggeling, and I. Urbančič, "High photon count rates improve the quality of super-resolution fluorescence fluctuation spectroscopy," J. Phys. D: Appl. Phys. **53**(16), 164003 (2020).
2. A. Benda, P. Kapusta, M. Hof, and K. Gaus, "Fluorescence spectral correlation spectroscopy (FSCS) for probes with highly overlapping emission spectra," Opt. Express **22**(3), 2973–2988 (2014).
3. A. J. García-Sáez and P. Schwille, "Fluorescence correlation spectroscopy for the study of membrane dynamics and protein/lipid interactions," Methods **46**(2), 116–122 (2008).
4. K. Bacia, I. V. Majoul, and P. Schwille, "Probing the endocytic pathway in live cells using dual-color fluorescence cross-correlation analysis," Biophys. J. **83**(2), 1184–1193 (2002).
5. J. Ries, S. Chiantia, and P. Schwille, "Accurate determination of membrane dynamics with line-scan FCS," Biophys. J. **96**(5), 1999–2008 (2009).
6. E. Haustein and P. Schwille, "Fluorescence correlation spectroscopy: novel variations of an established technique," Annu. Rev. Biophys. Biomol. Struct. **36**(1), 151–169 (2007).
7. R. Machán and M. Hof, "Recent developments in fluorescence correlation spectroscopy for diffusion measurements in planar lipid membranes," Int. J. Mol. Sci. **11**(2), 427–457 (2010).
8. P. Schwille, J. Korlach, and W. W. Webb, "Fluorescence correlation spectroscopy with single-molecule sensitivity on cell and model membranes," Cytometry **36**(3), 176–182 (1999).
9. L. C. Hwang, M. Gösch, T. Lasser, and T. Wohland, "Simultaneous multicolor fluorescence cross-correlation spectroscopy to detect higher order molecular interactions using single wavelength laser excitation," Biophys. J. **91**(2), 715–727 (2006).
10. B. Kannan, L. Guo, T. Sudhaharan, S. Ahmed, I. Maruyama, and T. Wohland, "Spatially resolved total internal reflection fluorescence correlation microscopy using an electron multiplying charge-coupled device camera," Anal. Chem. **79**(12), 4463–4470 (2007).
11. K. Bacia, S. A. Kim, and P. Schwille, "Fluorescence cross-correlation spectroscopy in living cells," Nat. Methods **3**(2), 83–89 (2006).
12. S. Ly, R. Altman, J. Petrlova, Y. Lin, S. Hilt, T. Huser, T. A. Laurence, and J. C. Voss, "Binding of apolipoprotein E inhibits the oligomer growth of amyloid-β peptide in solution as determined by fluorescence cross-correlation spectroscopy," J. Biol. Chem. **288**(17), 11628–11635 (2013).

13. L. Wawrezinieck, H. Rigneault, D. Marguet, and P.-F. Lenne, "Fluorescence correlation spectroscopy diffusion laws to probe the submicron cell membrane organization," Biophys. J. **89**(6), 4029–4042 (2005).
14. L. C. Hwang and T. Wohland, "Recent advances in fluorescence cross-correlation spectroscopy," Cell Biochem. Biophys. **49**(1), 1–13 (2007).
15. E. Zamir, C. Frey, M. Weiss, S. Antona, J. P. Frohnmayer, J.-W. Janiesch, I. Platzman, and J. P. Spatz, "Reconceptualizing fluorescence correlation spectroscopy for monitoring and analyzing periodically passing objects," Anal. Chem. **89**(21), 11672–11678 (2017).
16. S. Christie, X. Shi, and A. W. Smith, "Resolving membrane protein–protein interactions in live cells with pulsed interleaved excitation fluorescence cross-correlation spectroscopy," Acc. Chem. Res. **53**(4), 792–799 (2020).
17. M.J. Kaliszewski, X. Shi, Y. Hou, R. Lingerak, S. Kim, P. Mallory, and A.W. Smith, "Quantifying membrane protein oligomerization with fluorescence cross-correlation spectroscopy," Methods **140-141**, 40–51 (2018).
18. J. Wang, X. Huang, H. Liu, C. Dong, and J. Ren, "Fluorescence and Scattering Light Cross Correlation Spectroscopy and Its Applications in Homogeneous Immunoassay," Anal. Chem. **89**(10), 5230–5237 (2017).
19. J. He, S.-M. Guo, and M. Bathe, "Bayesian approach to the analysis of fluorescence correlation spectroscopy data I: theory," Anal. Chem. **84**(9), 3871–3879 (2012).
20. A. Tcherniak, C. Reznik, S. Link, and C. F. Landes, "Fluorescence correlation spectroscopy: criteria for analysis in complex systems," Anal. Chem. **81**(2), 746–754 (2009).
21. P. Schwille, F. J. Meyer-Almes, and R. Rigler, "Dual-color fluorescence cross-correlation spectroscopy for multicomponent diffusional analysis in solution," Biophys. J. **72**(4), 1878–1886 (1997).
22. J. Rika and T. Binkert, "Direct measurement of a distinct correlation function by fluorescence cross correlation," Phys Rev A Gen Phys. **39**(5), 2646–2652 (1989).
23. F. Bestvater, Z. Seghiri, M. S. Kang, N. Gröner, J. Y. Lee, K.-B. Im, and M. Wachsmuth, "EMCCD-based spectrally resolved fluorescence correlation spectroscopy," Opt. Express **18**(23), 23818–23828 (2010).
24. M. Burkhardt, K. G. Heinze, and P. Schwille, "Four-color fluorescence correlation spectroscopy realized in a grating-based detection platform," Opt. Lett. **30**(17), 2266–2268 (2005).
25. M. J. R. Previte, S. Pelet, K. H. Kim, C. Buehler, and P. T. C. So, "Spectrally resolved fluorescence correlation spectroscopy based on global analysis," Anal. Chem. **80**(9), 3277–3284 (2008).
26. V. Dunsing, A. Petrich, and S. Chiantia, "Multicolor fluorescence fluctuation spectroscopy in living cells via spectral detection," eLife **10**, e69687 (2021).
27. B. K. Müller, E. Zaychikov, C. Bräuchle, and D. C. Lamb, "Pulsed interleaved excitation," Biophys. J. **89**(5), 3508–3522 (2005).
28. J. Hendrix and D. C. Lamb, "Pulsed interleaved excitation: principles and applications," Methods Enzymol. **518**, 205–243 (2013).
29. M. Burkhardt and P. Schwille, "Electron multiplying CCD based detection for spatially resolved fluorescence correlation spectroscopy," Opt. Express **14**(12), 5013–5020 (2006).
30. A. M. Kabbani and C. V. Kelly, "Nanoscale Membrane Budding Induced by CTxB and detected via polarized localization microscopy," Biophys. J. **113**(8), 1795–1806 (2017).
31. S.L. Veatch, "Electro-formation and fluorescence microscopy of giant vesicles with coexisting liquid phases," In: TJ McIntosh, ed. *Lipid Rafts*. Humana Press, Totowa, NJ. pp. 59–72 (2007).
32. A. M. Kabbani and C. V. Kelly, "The detection of nanoscale membrane bending with polarized localization microscopy," Biophys. J. **113**(8), 1782–1794 (2017).
33. X. Woodward, E. E. Stimpson, and C. V. Kelly, "Single-lipid tracking on nanoscale membrane buds: The effects of curvature on lipid diffusion and sorting," Biochimica et Biophysica Acta (BBA) - Biomembranes. **1860**(10), 2064–2075 (2018).
34. J. A. Julien, A. L. Pellett, S. S. Shah, N. J. Wittenberg, and K. J. Glover, "Preparation and characterization of neutrally-buoyant oleosin-rich synthetic lipid droplets," Biochim Biophys Acta Biomembr. **1863**(8), 183624 (2021).
35. M. Kamata, Y. Takaba, Y. Taguchi, and Y. Nagasaka, "Rapid and label-free sensing of intermolecular interactions using compact optical diffusion sensor," Int. J. Heat and Mass Transfer. **133**, 73–79 (2019).
36. W. Schrimpf, V. Lemmens, N. Smisdom, M. Ameloot, D.C. Lamb, and J. Hendrix, "Crosstalk-free multicolor RICS using spectral weighting," Methods **140-141**, 97–111 (2018).
37. A. M. Kabbani, X. Woodward, and C. V. Kelly, "Revealing the effects of nanoscale membrane curvature on lipid mobility," Membranes **7**(4), 60 (2017).
38. V. Buschmann, B. Krämer, F. Koberling, P. GmbH, R. Macdonald, and S. Rüttinger, 2009, Quantitative FCS: Determination of the Confocal Volume by FCS and Bead Scanning with the MicroTime 200. 1.
39. P. Kapusta, R. Macháň, A. Benda, and M. Hof, "Fluorescence Lifetime Correlation Spectroscopy (FLCS): concepts, applications and outlook," Int J Mol Sci. **13**(12), 12890–12910 (2012).
40. M. L. Blades, E. Grekova, H. M. Wobma, K. Chen, W. C. W. Chan, and D. T. Cramb, "Three-color fluorescence cross-correlation spectroscopy for analyzing complex nanoparticle mixtures," Anal. Chem. **84**(21), 9623–9631 (2012).